Supplementary Note 1: Sources of artefacts in super-resolution microscopy

Super-resolution microscopy comprises a range of powerful techniques with the potential to provide novel insights into cell and molecular processes by overcoming the diffraction limit of conventional light microscopy. However, super-resolution approaches are prone to artefacts of differing source, severity and extent. They can originate from optical aberrations [26–28]; sample preparation [28–31]; reconstruction algorithms [5,29,31]; and imaging conditions [27,28,31]. These referenced papers all provide thorough descriptions of specific artefacts, how they arise, and preventative measures that can be taken. It is important to understand how these frequently-encountered artefacts can be conveyed by NanoJ-SQUIRREL.

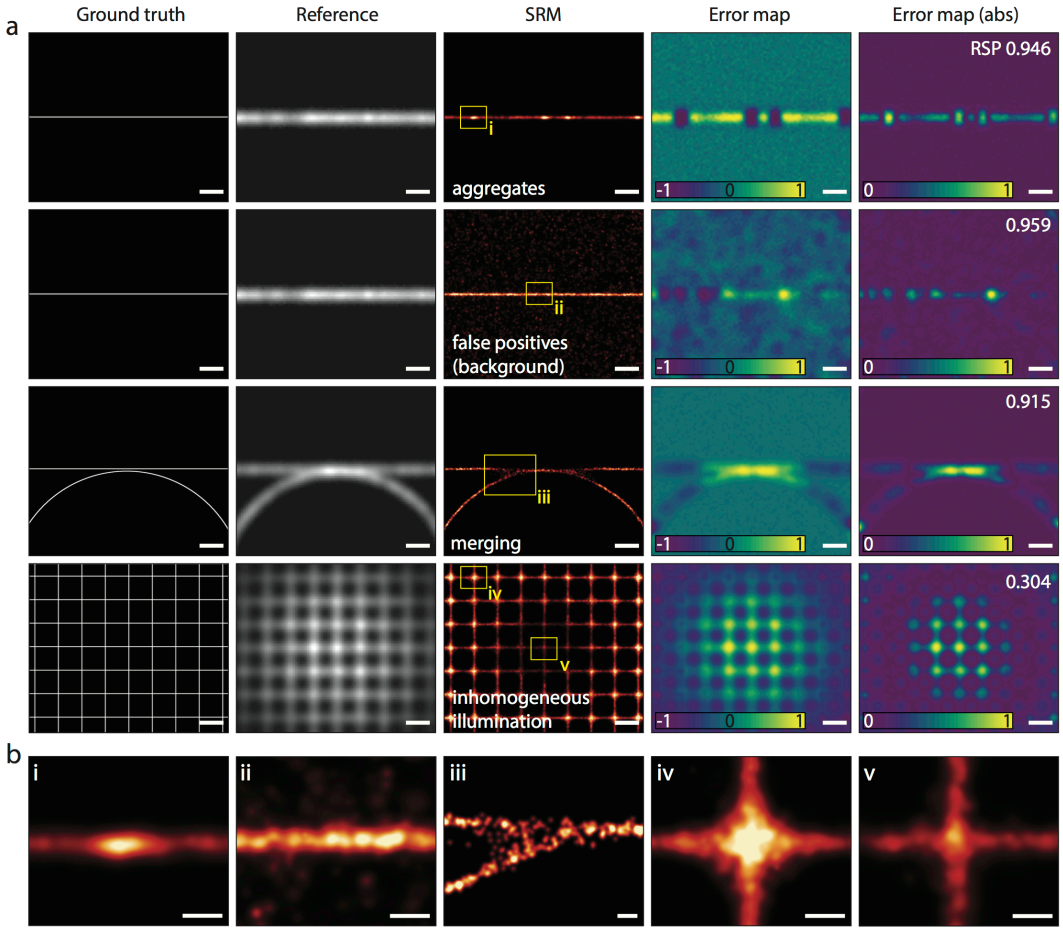

Fig. S1. Frequently encountered artefacts in super-resolution microscopy and error mapping via SQUIRREL. a) Ground truth (first column) and corresponding reference image (second column) of artificial structures with typical artefacts in the reconstructed super-resolution microscopy (SRM) image (third column). Here localization microscopy was used to generate the SRM, but these artefacts are not necessarily specific to this super-resolution modality. Error maps with normalized relative and absolute errors (fourth and fifth columns) show discrepancies between the SRM and reference image. Scale bars = 1μm. **b)** Enlarged views of typical artefacts corresponding to the boxed regions in the SRM images. Scale bars = 200nm. Figure represents simulated information emulating data from 4 independent experimental acquisitions.

For this purpose we generated a series of simulated super-resolution images containing a range of different artefacts and analysed them using SQUIRREL (Fig. S1). In Fig. S1, the first row includes aggregates (magnified in Fig. S1bi) in the super-resolution image that form local high intensity regions. In the relative error map these show up as error regions with a negative intensity mismatch while the rest of the filament is under-represented due to intensity normalization. The second row includes false positives (Fig. S1bii) which appear as positive- or negative-signed errors in the relative error map depending on whether they fall onto the structure or not. The third row shows the merging effect (Fig. S1biii) often observed in closely juxtaposed filaments. This effect is exacerbated by poor temporal separation of events, i.e. overlapping signal. The fourth row shows a regular grid with high illumination in the centre and decreasing illumination towards the edges (Fig. S1biv-v). Since the blinking behaviour is dependent on illumination intensity, localizations at the centre are better separated temporally than at the edges. As a result, localization density is lower in the centre, giving the impression of brightness inversion compared to the reference image. Since SQUIRREL is sensitive to differences in signal intensity,

the algorithm will rate this SRM image poorly, particularly in the centre.

One of the most common causes of artefacts in super-resolution microscopy is poor sample preparation, including unsuitable labelling density, use of aggregate-forming labels, or non-specific labelling. Label aggregates can appear as ‘hot spots’ in images, while unspecific signal will result in false positives or high background in images (Fig. S1 "aggregates" and "false positives"; Fig. 2 solid and dashed cyan boxes). Both types of artefact are highlighted in error maps following SQUIRREL analysis. Structural aberrations (artificial creation, disappearance, or merging of structures) are also common as artefacts, and can be due to fluorophore bleaching (SIM and STED), reconstruction algorithm artefacts (SIM and SMLM) or inappropriate imaging conditions and acquisition protocols regardless of super-resolution modality. For example, in SMLM optimal imaging conditions are required to ensure sufficient spatial separation of single molecule events, especially in regions of dense target structure, such as proximal or overlapping filaments [28,31]. Failure to achieve this typically results in artefactual widening of filaments at their intersection, or a blurring effect if filaments are in very close proximity (Fig. S1 “merging”; Fig. 2, solid yellow box). Again, these defects can be successfully highlighted using SQUIRREL.

Optical aberrations and image quality corruption by drift or vibrations might go unnoticed by a novice user if no solid image quality metrics are employed. Sample drift can usually be analytically corrected, post-acquisition, by use of fiducials or cross-correlation-based adjustments, and careful examination of resulting super-resolution images. However, optical aberrations, such as inhomogeneous illumination, are much harder to identify and can originate from fundamental flaws in the system optics or day-to-day variations such as improper stage alignment. If undetected, these aberrations can severely corrupt the quality of super-resolution images. In SMLM datasets, for example, fluorophore blinking statistics depend largely on illumination intensity and any inhomogeneity across the field of view is likely to introduce artefacts by increasing the variability of fluorophore behaviour. A simulated image showing the effect of such variability on a super-resolution image, along with the SQUIRREL error map, is shown in (Fig. S1 “inhomogeneous illumination”).

Systematic classification of all types and origins of possible image artefacts would be an enormous task, as they are method-, sample- and user-dependent. As shown with the selected examples above, NanoJ-SQUIRREL does not specifically identify the type or source of artefacts in an image, but rather provides metrics to compare super-resolution images acquired under different conditions as well as an error map where one can easily inspect the locations of defects in any single image. This allows a user - novice or expert - to easily identify the presence of image artefacts and rely on the extensive literature available on their method of choice to pinpoint the exact nature of the artefact, and/or explore the specific protocol being followed to identify their origin and how best to address it. Likewise, use of NanoJ-SQUIRREL allows the objective determination of the optimal image acquisition protocols and analytical approaches to best cope with already-identified errors or artefacts, as demonstrated in Figs. 3, S11 and S10. Finally, if a user wants to draw biological conclusions from a super-resolution image then SQUIRREL can highlight regions that are inappropriate for inclusion in any further data analysis.

Supplementary Note 2: Extracting the Resolution Scaling Function

The Resolution Scaling Function (RSF) can be estimated in 3 different ways: A) automatically during the error map generation procedure; B) approximated to the point spread function (PSF) of the microscope; C) derived when the reference PSF and super-resolution PSF are known. These processes are described below:

A. Automatic RSF generation. For the majority of cases, a symmetric normalized Gaussian function $\boldsymbol{G(x,y)}$ (Eq. S1) provides a good numerical approximation to the RSF. Studies have shown that the PSFs of widefield, TIRF, laser scanning confocal microscopy and spinning disk microscopy can be, in a simplified manner, approximated to Gaussian functions [8,32,33]. Similarly, in super-resolution methods, the final images generally present a Gaussian-like PSF [8,33–35]. The RSF in itself is expected to be a function that by convolution would convert the super-resolution PSF (PSF_S) into the reference image PSF (PSF_D) (Eq. S2); if both of these are assumed to follow a Gaussian distribution, then the RSF will be well approximated by a Gaussian. Although the $\boldsymbol{\sigma}$ value describing the Gaussian RSF is unknown, it can be estimated during optimisation. Supplementary Note 3, stage B provides an analytical description of this process.

$$G(x,y) = \frac{1}{2\pi\sigma^2} e^{\left(-(x^2+y^2)/(2\sigma^2)\right)} \tag{S1}$$

$$PSF_D \approx PSF_S \otimes RSF \tag{S2}$$

B. Approximation of RSF to the PSF. When the resolution of the super-resolution dataset is considerably high (<30nm, ~10-fold improvement upon the diffraction limit), the PSF of the microscope provides a good approximation of the RSF. In such cases, the user will be able to provide a PSF rendering to the error map calculation procedure, as a proxy to the RSF. For simplicity, we provide as part of NanoJ-SQUIRREL an algorithm capable of extracting a model PSF from an image composed of sparse sub-diffraction PSF-like particles (Fig. S2). Alternatively, the user can also derive a theoretical PSF based on a diffraction model; the PSF Generator ImageJ-plugin [20] is an excellent tool in such cases, providing PSF rendering capability and maintaining an extensive library of PSF models.

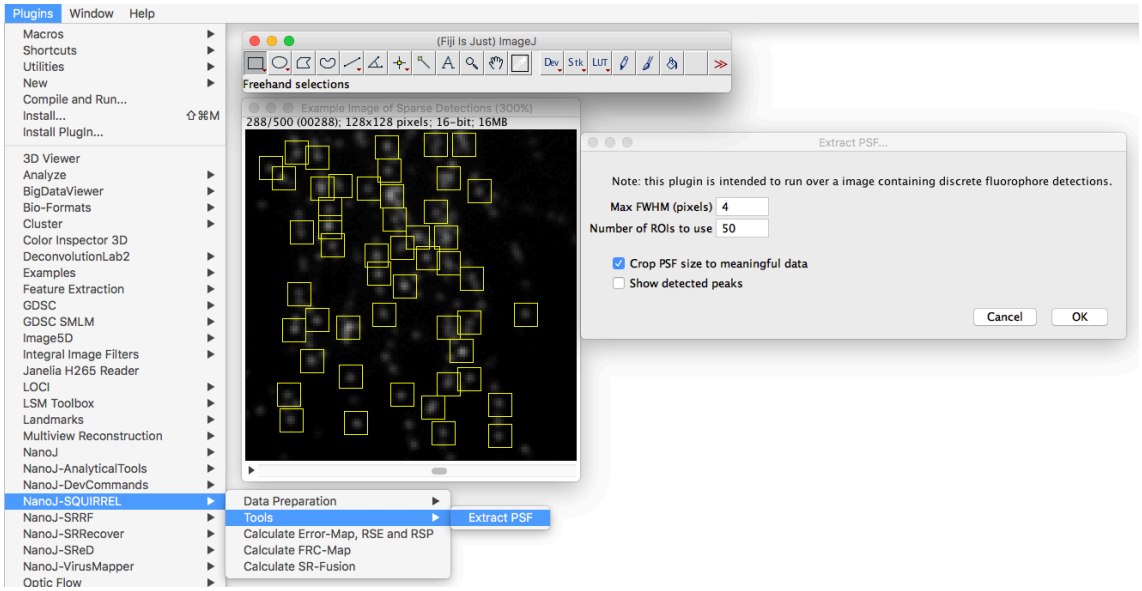

Fig. S2 The 'Extract PSF' algorithm, part of NanoJ-SQUIRREL. This method searches for peaks in the image (local maxima) and fits a 2D Gaussian function (Eq. S1) to each (of varying amplitude, centre, background and σ). This fitting estimates the centre of each peak with a sub-pixel accuracy. Each peak is then extracted, aligned and re-rendered in a list of images representing all the detected peaks. An initial estimate is generated by an average projection of all extracted peaks. A final estimate is then regenerated by a weighted average projection where each peak component is weighted by its Pearson correlation coefficient against the previous average projection.

C. Derived when the reference PSF and super-resolution PSF are known. Through Eq. S2, the RSF matrix can be estimated if both PSF_D and PSF_S are known. These two last matrices can be extracted either from real data, or estimated by underlying analytical models. For a noise free case, the calculation of the RSF can be done in Fourier space, by calculating the inverse transform of the division between the Fourier transformed PSF_D and Fourier transformed PSF_S. This calculation is not included in the NanoJ-SQUIRREL software package.

Supplementary Note 3: The SQUIRREL algorithm

The SQUIRREL method is provided as part of the NanoJ high-performance super-resolution data analysis package. It takes advantage of analytical features associated with NanoJ-SRRF [14] and NanoJ-VirusMapper [36]. The process of estimating an error map via SQUIRREL is divided in 3 subsequent steps represented in Fig. 1a and described below. The following notation will be used to denote the different images during this process:

- I_D: diffraction-limited reference image
- RSF: resolution scaling function
- I_{RSF}: resolution scaling function integrated over finite pixels
- I_S: original super-resolution image
- $I_{ST} = I_S(x - \Delta x, y - \Delta y)$: super-resolution image registered to reference image
- $I_{ST\gamma} = I_{ST} \times \alpha + \beta$: registered super-resolution image following linear intensity rescaling.

A. Registration of super-resolution reconstructions against the reference image. The first step of registration is the estimation of the lateral mismatch $\Delta x, \Delta y$, through cross-correlating the reference and the super-resolution images. The translation is needed to correct for aberrant shifts in the super-resolution image I_S arising from uncorrected sample drift, differences between the optical path used to collect the reference diffraction-limited image I_D and super-resolution image I_S, or offsets introduced by reconstruction algorithms. For this purpose, the cross-correlation is calculated through a fast Hartley transform (FHT), taking advantage of the threaded Parallel Colt library [37]. $\Delta x, \Delta y$ can then be estimated by calculating the spatial difference between the coordinates of the correlation matrix peak intensity value and its geometric centre. To detect the coordinates of the peak correlation value, we selectively upscale the correlation matrix via bi-cubic spline interpolation [38] and find its maximum. This process has been previously described in [39]. Finally, we employ a bi-cubic spline translation of the super-resolution image to maximise its overlap to the reference image to produce I_{ST} (Eq. S3).

$$I_{ST} = I_S(x - \Delta x, y - \Delta y) \tag{S3}$$

B. Image intensity rescaling and RSF estimation. The intention of this step is to linearly rescale the intensity of the super-resolution estimate I_S and convolve it with I_{RSF} in a manner that will maximise the similarity of its intensity range to that of the reference image I_D. To do so, the unknown variables α and β defining the intensity rescaling need to be estimated to generate $I_{ST\gamma}$ (Eq. S4).

$$I_{ST\gamma}(\alpha, \beta) = I_{ST} \times \alpha + \beta \tag{S4}$$

Additionally, if an RSF is not input, the SQUIRREL algorithm will automatically estimate its matrix by an approximation to a 2D Gaussian function (Eq. S5) of unknown σ. Similarly to [40], we integrate the Gaussian function over finite pixels (Eq. S6-S7). The estimation of these two (if then RSF is known) or three variables (if the RSF is unknown) is achieved in SQUIRREL through a highly threaded implementation of a Particle Swarm Optimiser (PSO) [41,42]. PSO optimisation is a derivative-free, metaheuristic optimisation approach taking few assumptions about the optimisation problem posed and is capable of searching a large space of candidate solutions. Equation S8 defines the least-squares minimisation, where the result of $I_{ST\gamma}(\alpha, \beta) \otimes I_{\mathrm{RSF}}(\sigma)$ is scaled down to the same width and height as I_D by pixel averaging prior to their subtraction.

$$\mathrm{RSF}(x, y) = \frac{1}{2\pi\sigma^2} e(-(x^2 + y^2)/(2\sigma^2)) \tag{S5}$$

$$I_{\mathrm{RSF}}(x, y) = \Delta E_x(x, y) \Delta E_y(x, y) \tag{S6}$$

$$\begin{cases} \Delta E_x(x, y) \equiv \frac{1}{2}\mathrm{erf}\left(\frac{x+0.5}{\sqrt{2}\sigma}\right) - \frac{1}{2}\mathrm{erf}\left(\frac{x-0.5}{\sqrt{2}\sigma}\right) \\ \Delta E_y(x, y) \equiv \frac{1}{2}\mathrm{erf}\left(\frac{y+0.5}{\sqrt{2}\sigma}\right) - \frac{1}{2}\mathrm{erf}\left(\frac{y-0.5}{\sqrt{2}\sigma}\right) \end{cases} \tag{S7}$$

$$\text{Joint Optimisation } \alpha, \beta, \sigma\text{: } \mathrm{argmin}_{\alpha,\beta,\sigma} \left\| I_D - I_{ST\gamma}(\alpha, \beta) \otimes I_{\mathrm{RSF}}(\sigma) \right\|_2 \tag{S8}$$

C. Calculation of error map, RSE and RSP. The process of error mapping starts by the calculation of I_{RS}, the image created by applying the RSF to the super-resolution image (Eq. S9).

$$I_{RS} = [I_{ST} \times \alpha + \beta] \otimes \mathrm{RSF} \tag{S9}$$

$$= I_{\mathrm{ST}\gamma}(\alpha, \beta) \otimes I_{RSF}(\sigma) \tag{S10}$$

The global similarity between I_{RS} and the reference diffraction-limited image I_D can be calculated through a root-mean-square error (Eq. S11), named RSE for Resolution Scaled Error, and a Pearson correlation coefficient, named RSP for Resolution Scaled Pearson coefficient (Eq. S12). Here n represents the total number of pixels (where necessary, the dimensions of I_{RS} are scaled to match those of I_D), $\overline{I_D}$ the average value of I_D and $\overline{I_{RS}}$ the average value of I_{RS}.

$$\mathrm{RSE} = \sqrt{\frac{\sum_{x,y}\left(I_D(x,y) - I_{RS}(x,y)\right)^2}{n}} \tag{S11}$$

$$\mathrm{RSP} = \frac{\sum_{x,y}(I_D(x,y) - \overline{I_D})(I_{RS}(x,y) - \overline{I_{RS}})}{\sqrt{\sum_{x,y}(I_D(x,y) - \overline{I_D})}\sqrt{\sum_{x,y}(I_{RS}(x,y) - \overline{I_{RS}})}} \tag{S12}$$

The error map M is the pixel-wise absolute difference between I_D and I_{RS} (Fig. 1a, Eq. S13). While other metrics could be adapted for super-resolution images, such as the structural similarity index (SSIM) [43], here we show that the RSE, RSP and error map provide a robust, detailed evaluation of super-resolution image quality suitable for optimising super-resolution experiments.

$$M(x,y) = \left| I_D(x,y) - I_{RS}(x,y) \right| \tag{S13}$$

Supplementary Note 4: Application of SQUIRREL to SIM data

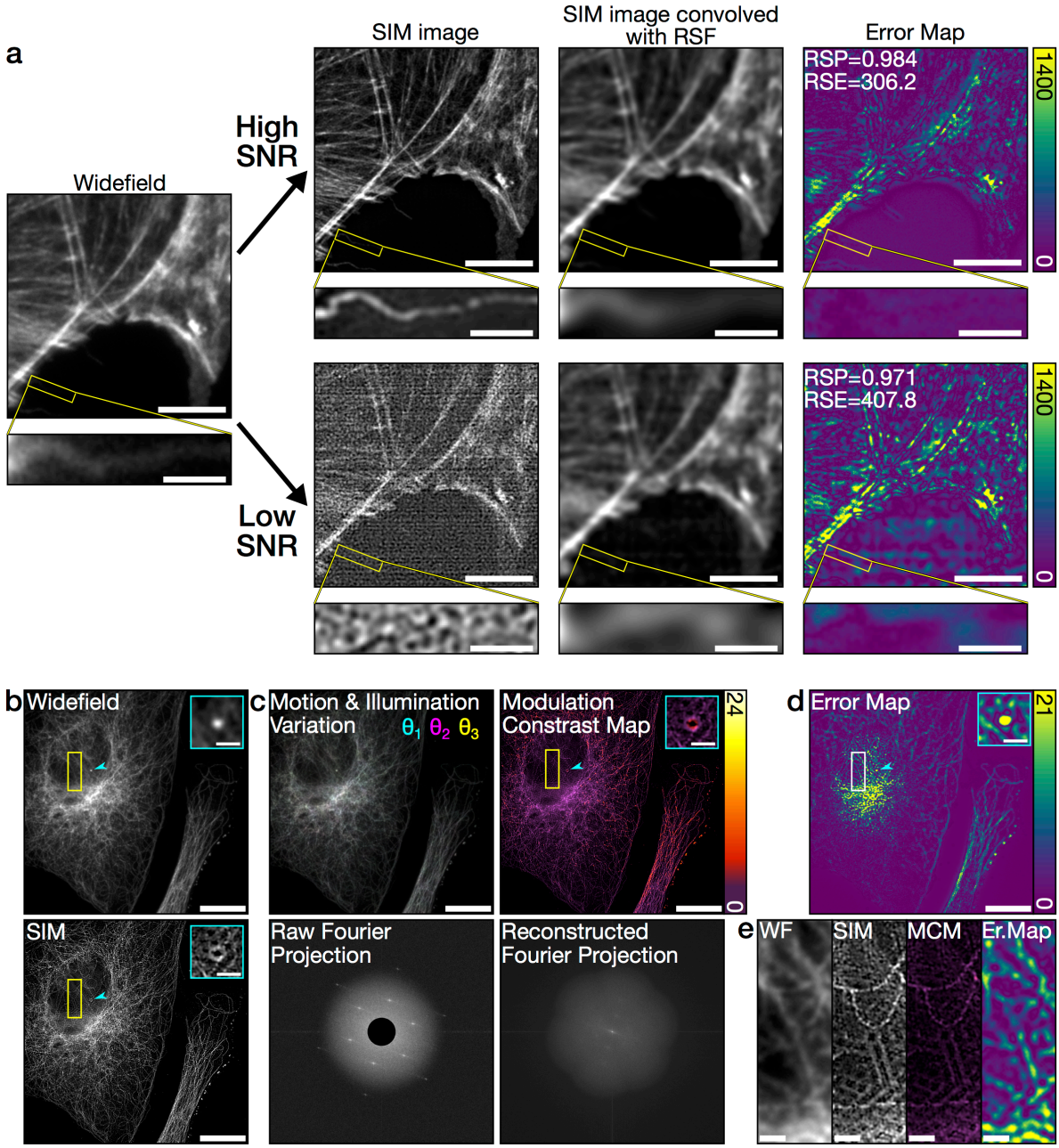

Fig. S3. Application of SQUIRREL analysis to SIM data. a) Actin imaged using standard widefield microscopy followed by SIM at two different laser intensities. SQUIRREL analysis was run on the two SIM images, both using the widefield image as the reference. With an increased laser intensity a high signal-to-noise ratio (SNR) is achieved (top row), yielding more structural detail in the SIM image than with a decreased laser intensity (bottom row). Fine details are lost (inset) and artefactual background patterning (error map) becomes apparent at low SNR. Main image scale bars = 5 μm, inset scale bars = 1 μm. **b)** Microtubules imaged by widefield microscopy followed by SIM. Scale bars = 10 μm. Top right insets show the area indicated by the cyan arrowhead, scale bar 1 μm. **c)** Examples of output images from running SIMcheck [10] on the reconstructed SIM image in **b** and its corresponding raw data. Scale bars = 10 μm. **d)** SQUIRREL error map of the images in **b**. Scale bar = 10 μm. **e)** Magnified inset corresponding to the yellow/white boxed region. MCM = Modulation Contrast Map, Er.Map = error map. Scale bars = 1 μm. Figure represents a single data acquisition.

To demonstrate that SQUIRREL is applicable across different super-resolution imaging modalities, we used it to analyse SIM data (Fig. S3). SIM acquisitions of actin in fixed cells were performed at two different laser intensities (leading to one low- and one high-SNR data set) and from these SIM images were reconstructed (Fig. S3a). SQUIRREL analysis of these images yielded poorer RSP and RSE values in the low SNR case compared to the high SNR case, and the error map successfully highlighted discrepancies between each reconstructed SIM image and the widefield reference. This allowed for identification of a filament that was successfully resolved in the high SNR image but was absent in the low SNR image. SIM is one of the few areas in super-resolution microscopy where there is already a robust open-source toolbox for

assessing image quality, SIMcheck [10]. To compare the types of information obtainable from SIMcheck and SQUIRREL, SIM and widefield images of microtubules in fixed cells were acquired (Fig. S3b) and the quality of the SIM data was analysed using both SIMcheck (Fig. S3c) and SQUIRREL (Fig. S3d). Four example output images from SIMcheck are shown in Fig. S3c, and these provide important SIM-specific information. The bright, symmetric peaks in the 'Raw Fourier Projection' image suggest good quality raw data; the symmetry of the 'Reconstructed Fourier Projection' image suggests that resolution is consistent across the three grating angles, although the presence of faint dots indicates that there is periodic patterning in the image; the mainly white appearance of the 'Motion and Intensity Variation' image indicates that there is minimal drift or intensity differences between the three grating angles (θ_1, θ_2, θ_3); the 'Modulation Contrast Map' indicates inhomogeneities in the contrast to noise ratio of the reconstructed SIM image. SIMcheck also provides quality metrics, and for this image the MCNR (modulation contrast-to-noise ratio) metric has a low value indicative of poor image quality. This is reflected in the low values in the Modulation Contrast Map. The SQUIRREL error map is shown in Fig. S3d; taking the SQUIRREL error map alongside the SIMcheck information, the areas of high error in SQUIRREL mostly correlate to regions with poor modulation contrast. This is further seen in the Fig. S3e, where SQUIRREL highlights that there are filaments absent from the SIM image and SIMcheck indicates that this area has a low modulation contrast. The good quality of the raw Fourier projection and motion and intensity variation images indicate that the low modulation contrast is likely due to local noise contributions such as out-of-focus fluorescence rather than a fault with the optical system itself. However, SQUIRREL also shows that modulation contrast may be misleading in some cases. For example, the bright aggregate highlighted with an arrowhead appears to have better modulation contrast than the surrounding objects but appears as a high error region in SQUIRREL. This is because the reconstruction algorithm has incorrectly rendered this bright object as a ring. SQUIRREL and SIMcheck can thus be used in tandem to highlight artefacts in SIM images and formulate strategies for reducing them in future acquisitions.

Supplementary Note 5: The influence of focal depth mismatch between the reference and super-resolution images for SQUIRREL error maps

The capacity of SQUIRREL to accurately highlight errors in super-resolution reconstructions is based on the assumption that both reference and super-resolution images represent the same focal plane. However for localization microscopy (and image-based approaches such as SOFI and SRRF), the underlying analytical process may provide some degree of optical sectioning and, in the case of localization microscopy, a bias toward incorrect particle detection away from the focal plane. To verify the effects of out-of-focus information and optical sectioning, and validate their possible disruptive influence in error map calculation, we have designed three studies. The first study uses datasets featuring experimentally-acquired PSFs, the second study uses PSFs obtained from the Born and Wolf optical model, and the third study uses fully experimentally-acquired 3D dSTORM data.

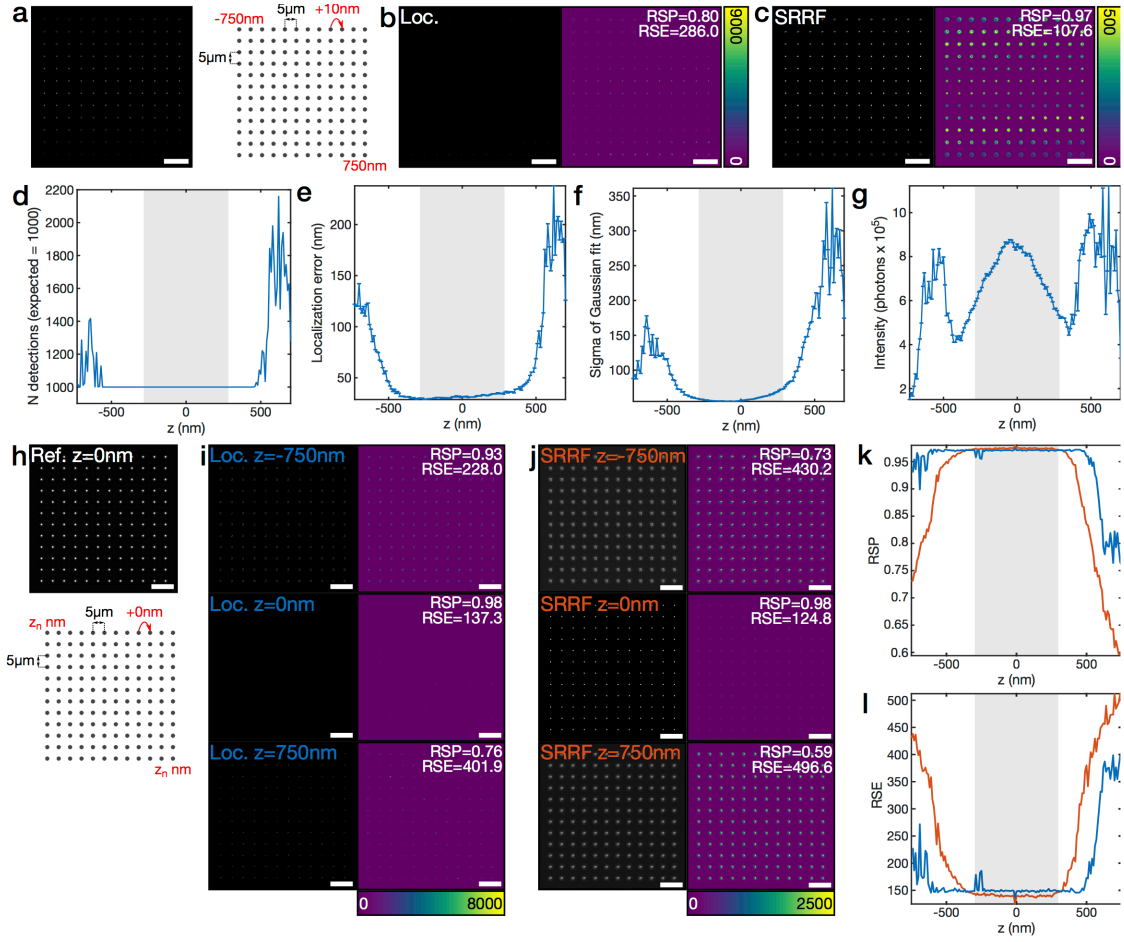

Fig. S4. Evolution of error with distance from focal plane for localization microscopy and SRRF. Synthetic datasets were created by rendering images of fluorescent beads at predefined z positions and in regular spaced x,y coordinates. Rendered PSFs are based on experimentally acquired PSFs, as used in the 2016 SMLMS challenge (see Methods), and have been re-rendered with a Gaussian-Poisson noise mixture model. **a)** shows a sample frame from the first dataset where the z position (red) increases from -750 nm (top left corner) to +750 nm (bottom right corner) and a schematic of the spacings in the image. **b)** shows a ThunderSTORM image (Loc. for localization) from n=1000 frames containing PSFs similar to those in **a**, and the corresponding error map against a widefield reference; **c)** shows the SRRF reconstruction and error map for the same dataset. **d)** shows how the number of ThunderSTORM detections varies per bead (and hence per z-position) for this 1000 frame dataset, **e)** shows the mean Euclidean distance between each localization and the centre of the nearest bead, **f)** shows the mean sigma of the fitted Gaussian for each localization, **g)** shows the mean number of photons at each bead position. . Error bars in **e-g** are s.e.m. with n equal to the number of detections at each position as plotted in **d**. A second dataset was created where all beads in a single frame were now in the same focal plane, and focal plane was varied by 10 nm from frame to frame. **h)** shows an example frame where all beads are at z=0 nm with a schematic of the spacing beneath (z_n = z-position for frame n in dataset). i) ThunderSTORM images of the first (z=-750 nm), middle (z=0 nm) and last (z=750 nm) frames in the dataset and the corresponding error maps when the in-focus widefield image **h** was used as the reference. **j)** is as in **i**, but with SRRF analysis. **k)** and **l)** show plots of the RSP and RSE, respectively, for each frame of the ThunderSTORM (blue) and SRRF (red) reconstructions when the in-focus frame (**h**) is used as the reference. All scalebars = 10 μm Grey shaded regions on plots indicate the central 600 nm which is approximately the range of the 'virtual light-sheet' as described in [44]. Panels **h-l** represent the evaluation of 1440 independently rendered PSFs.

For the first assay super-resolution images were reconstructed from a synthetic dataset, where images of non-blinking fluorescent beads acquired at z-positions ranging from -750 nm to +750 nm were regularly distributed (Fig. S4a) and subsequently analysed using localization microscopy (Fig. S4b) and SRRF (Fig. S4c). The error maps produced for these two methods are shown alongside the reconstructions; it can be seen that the localization microscopy image exhibits a lower RSP value than the SRRF image, and that the peak local errors in the SRRF image are an order of magnitude smaller than those in the localization microscopy image. This indicates that localization microscopy is more sensitive to out-of-focus molecules than SRRF, which conversely better preserves the spatial intensity distribution of the out-of-focus PSF. The sensitivity of localization microscopy to out-of-focus fluorescence has been recently discussed in depth [44]; in this work the authors show that localizations arising from regions beyond the central ~600 nm in z can be filtered out according to their widths and intensities. We replicated this result here by running localization microscopy on a dataset comprising 1000 frames with a distribution of beads imaged at different z-positions as shown in Fig. S4a. This confirmed that while localization microscopy successfully measured one detection per bead for z=0±500 nm, beyond this range there is a considerably increased probability of multiple detections per bead (Fig. S4d). Furthermore, we calculated the localization error against the true centre of each bead as a function of their z-position (Fig. S4e); this showed that, as expected, within a central ~600 nm (grey-banded region) there is minimal discrepancy between the location of the detection and the true position of the bead. The average width of the Gaussian fit used for localization also reached a minimum within the central ~600 nm (Fig. S4f), and the average intensity per detection also peaked in this region (Fig. S4g). Of note, for the highlighted 600 nm region, it becomes increasingly difficult to differentiate beads based on their 2D localization parameters.

Next, we sought to verify how error map and quality metric sensitivity correlates with increasing depth. To do this, a second dataset of bead images was generated. This time, each frame was populated with 144 bead images at the same focal position and z-position was changed between frames; here, super-resolution renderings of these frames (at z-positions again ranging from -750 nm to 750 nm) were error-mapped against an in-focus reference image (i.e. z=0 nm, Fig. S4h). Again, both localization microscopy (Fig. S4i) and SRRF (Fig. S4j) were used to produce super-resolution images, and SQUIRREL analysis was performed to get RSP (Fig. S4k) and RSE (Fig. S4l) metrics for images across the whole range of z-positions. Both algorithms displayed a peak RSP and minimum RSE near the focal plane as expected, with lower RSP/higher RSE values as distance from the focal plane increased. This was more noticeable for the SRRF images than the localization microscopy images; this was due to better preservation of relative intensity and true PSF shape in SRRF than in localization microscopy. The central z-range over which the RSP and RSE metrics remain largely constant coincides with the highlighted 600 nm region, indicating that within this focal volume there is negligible depth bias for SQUIRREL errors calculated against localization microscopy or SRRF images. This study represents the expected values obtained using common optical configurations used in 2D localization microscopy (e.g. 1.49 NA objective and 100-160 nm pixel sizes) and well-separated fluorophores (5 μm spacing here). However, deviation from these settings may lead to additional possible biases.

Taken together, these results indicate two important points to note when performing SQUIRREL analysis: RSF estimation for a dataset containing a wide range of z positions may not be optimal or accurate, and SQUIRREL will report errors associated with out-of-focus fluorescence more sensitively for super-resolution techniques that preserve the intensity distribution of out-of-focus fluorescence (such as SRRF) than for techniques (such as localization microscopy) where molecules are re-rendered as point sources.

A further simulated dataset was used to compare contributions of errors arising from out-of-focus regions with errors arising from structural defects. A structure was simulated at a linear tilt to the focal plane such that one end of the structure was 750 nm below the focal plane, the centre was in focus, and the other end was 750 nm above the focal plane, and SQUIRREL analysis was performed (Fig. S5). Firstly, a ‘defect-free’ single molecule data set was produced by simulating blinking molecules over the corresponding axial range using a Born and Wolf optical model [20]. This image sequence was analysed using ThunderSTORM to produce a realistic super-resolution image and then compared with a simulated widefield image of the same structure (Fig. S5a,c). The error map shows that the super-resolution reconstruction was, as expected, accurate for the in-focus regions of the structure in the middle of the image but in poor agreement with the out-of-focus regions of the sample. Next we investigated whether errors arising from out-of-focus fluorescence would mask errors within the focal plane. To do this, a deliberately artefactual single molecule data set was produced where periodic regions of the structure were absent; this was again reconstructed using ThunderSTORM analysis (Fig. S5b). The error map generated through comparison with the defect-free widefield image (Fig. S5c) clearly demonstrates that while the errors arising from out-of-focus fluorescence are still present, the errors resulting from structural mismatch are also readily identifiable as periodic peaks in the error map.

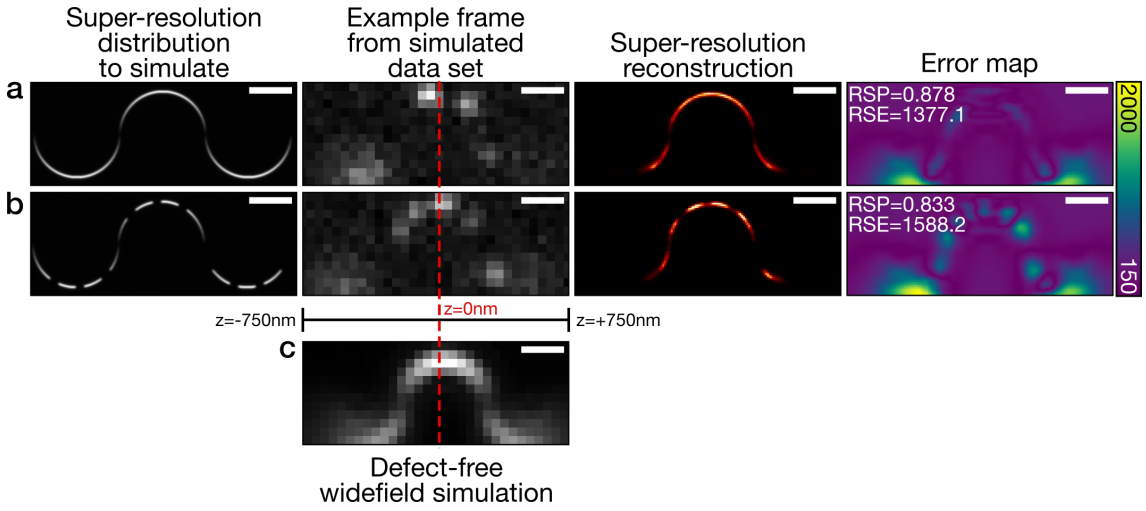

Fig. S5. Impact of out-of-focus fluorescence on error maps, RSP and RSE values. a) Test structure for defect-free super-resolution simulation; example frame from simulated single molecule data set where there is an axial tilt along the x-dimension; result of running the simulated data set through ThunderSTORM analysis; error map generated between the reconstructed image and a simulated defect-free widefield image (**c**). **b)** As in **a**, except here there are periodic defects in the super-resolution image which are not present in the widefield image. **c)** Defect-free widefield image produced of the tilted structure shown in **a**. Scale bars = 500 nm. Figure represents data from 1 of 10 similar independent simulations.

We next investigated the effect of a mismatch between the focal volume represented by the reference and super-resolution images used for SQUIRREL error map calculation in real data. Analysis was performed for images where there was a deliberate mismatch between the laser beam illumination angle (positioned at either widefield, HILO or TIRF) used for reference and super-resolution imaging (Fig. S6). Each super-resolution dSTORM acquisition was performed with a cylindrical lens in the detection path such that detected molecules could be localized in z to highlight any directional bias in SQUIRREL analysis. Three different illumination regimes were used for super-resolution data acquisition: widefield (WF; Fig. S6a), HILO (Fig. S6b) and TIRF (Fig. S6c). In addition to 3D super-resolution datasets, a 2D reference image was acquired at the same illumination angle as the super-resolution data, and a mercury lamp-illuminated ('Hg') WF image (using a different dichroic mirror to the laser path) was also acquired. Figure S6ai-vi shows enlarged insets of the WF super-resolution image corresponding to local high error areas. In the WF Ref. vs WF SR case, insets i and ii show areas of filament crossing where there are filament-merging artefacts and erroneous localizations between filaments. Inset iii shows error associated with what initially appeared to be a single bright filament, but upon closer inspection of the super-resolution image looks likely to be two filaments merged into one. None of these three regions appeared as high error regions when the Hg image was used as the reference; while filament crossing errors were still highlighted in the Hg Ref. vs WF SR error map (inset iv), the most prominent errors were from blurry out-of-focus regions (inset v) and regions with a large intensity mismatch (inset vi). Globally, however, the two error maps for the WF SR image showed similar error distributions with considerable error associated with the blurred top-right corner of the image. This example in particular highlights the effect of small differences in the light path between the super-resolution and reference images (i.e. a different filter cube).

However, for the HILO SR image there is a considerable difference in mapped error distributions between using the HILO reference and the Hg reference (Fig. S6b). In the HILO Ref. vs HILO SR error map there are high local errors associated with microtubule bundles (insets i and iii), but also in an area where there is large variation in the z-positions of the microtubules (inset ii). 90% of the detected molecules within inset ii fall within the z-range -300 nm to 370 nm (compared to -430 nm to -60 nm for inset i); while this appears to be within the negligible-bias 600 nm region demonstrated in Fig. S4, the area is dense with microtubules that will also corrupt detection and localization. While the Hg Ref. vs HILO SR map can highlight some local errors from microtubule merging and bundling (insets iv and v), the majority of the error is concentrated in a region that is beyond the range of effective HILO illumination (inset vi). Finally, the TIRF super-resolution error maps show the most striking example of error discrepancy between the two acquired reference images (Fig. S6c). Almost all of the local errors are concentrated on microtubule junctions and bundles in the TIRF Ref. vs TIRF SR error map (insets i-iii) whereas the difference in the illumination schemes in the Hg Ref. vs TIRF SR error map is dominant over any other errors (insets iv-vi). To summarise, SQUIRREL analysis will give the best accuracy in error reporting for the smallest possible focal volume (e.g. TIRF illumination). With increased focal volume, or a mismatch in the focal volumes of the reference and super-resolution images, the contributions of out-of-focus structures will be highlighted as errors and in extreme cases could even mask other structural artefacts. Therefore it is important for users to take these points into consideration when assessing error maps produced by SQUIRREL, and ascertain whether highlighted artefacts are arising from out-of-focus information or local errors from the super-resolution image production process.

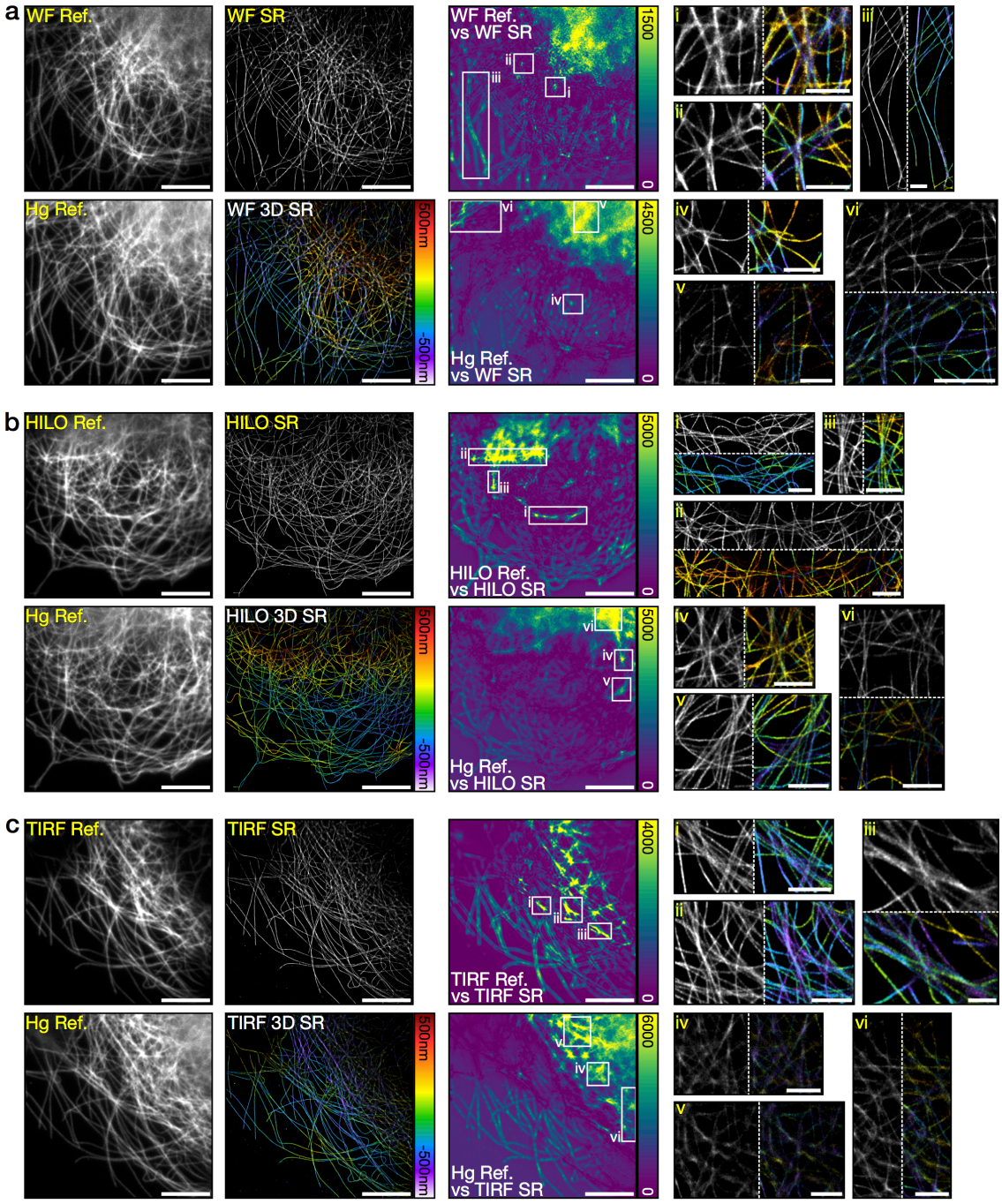

Fig. S6. Effect of focal volume mismatch between reference and super-resolution images on SQUIRREL error maps. First column: Reference ('Ref.') images taken in WF (**a**), HILO (**b**), and TIRF (**c**) illumination regimes (top) and reference images of the same region taken with mercury lamp widefield illumination ('Hg Ref.'). Second column: Super-resolution ('SR') images acquired with laser widefield illumination (WF) (**a**), HILO (**b**), and TIRF (**c**) displayed as 2D (greyscale) and 3D (depth colour-coded) renderings. Third column: Error maps between the super-resolution images and references taken with the same laser illumination angle (top) and error maps between the super-resolution images and the Hg references (bottom). Scale bars in first three columns = 10 µm. Fourth column: Enlarged 2D and 3D super-resolution renderings of the corresponding boxed regions in the error maps. Scale bars = 2 µm. Figure represents data from 1 of 5 independent experiments showing similar results.

Supplementary Note 6: Size and signal-to-noise sensitivity of SQUIRREL

To estimate the resolution scale to which SQUIRREL is able to identify super-resolution anomalies, we here designed a simulated super-resolution imaging experiment where controlled defects can be incorporated into a known structure. To this effect, we have simulated an 8-molecule ring structure where the separation between adjacent molecules (Δd) can be varied (Fig. S7a).

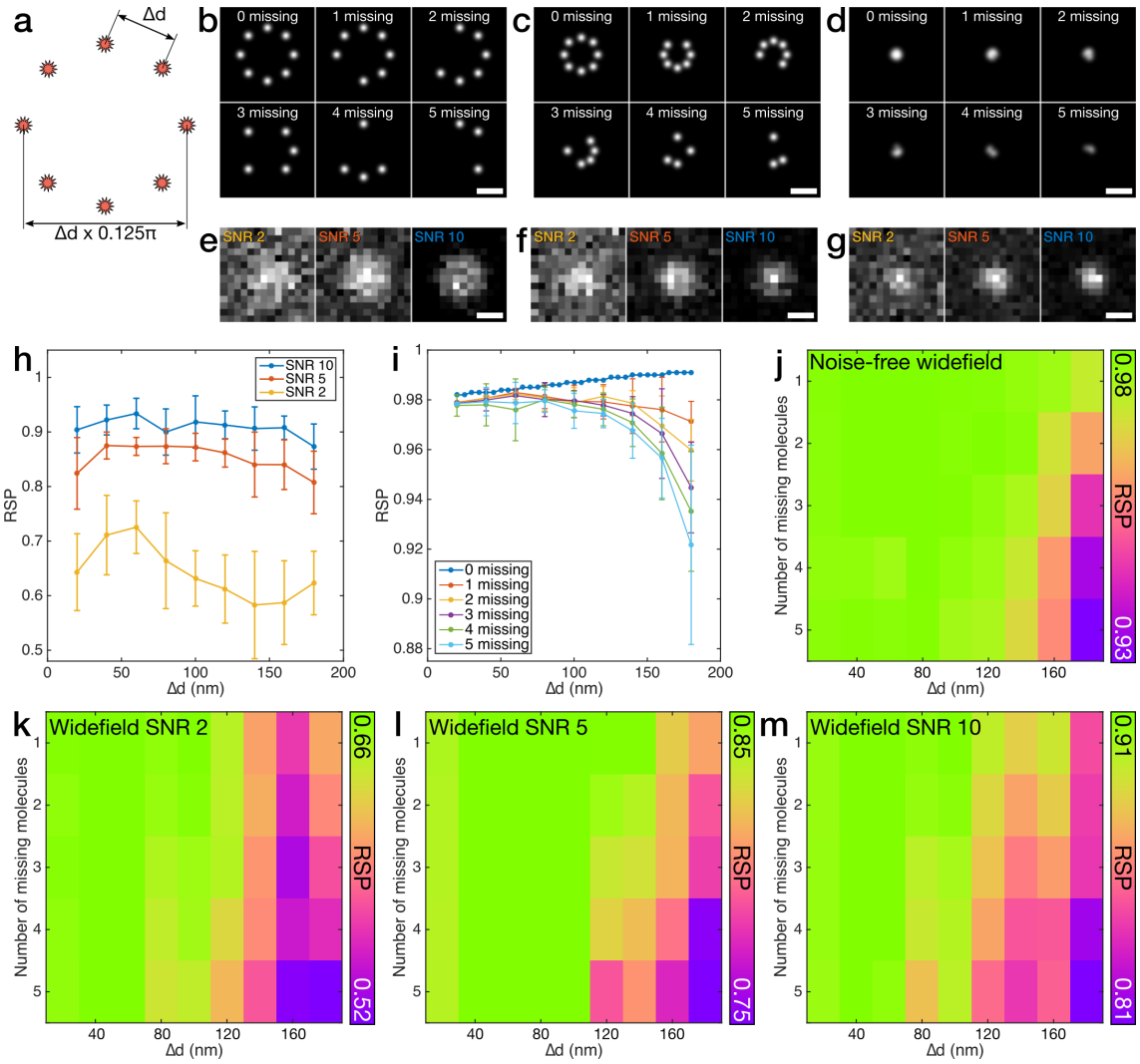

Fig. S7. Resolution and signal-to-noise sensitivity of SQUIRREL. a) Geometry of an 8-molecule ring structure for simulations, where Δd indicates the separation between adjacent molecules. **b-d)** Representative simulated super-resolution images with varying numbers of randomly removed molecules from the ring structure with Δd values of **b)** 160 nm, **c)** 100 nm, **d)** 20 nm, rendered with Gaussian distributions of σ=20 nm. Scale bars = 200 nm. **e-g)** Representative simulated widefield images of rings with no molecules missing at three different signal-to-noise ratios (SNR) for Δd values of **e)** 160 nm, **f)** 100 nm, **g)** 20 nm, where the widefield PSF is approximated to a Gaussian distribution of σ=135 nm. Scale bars = 200 nm. **h)** RSP values generated by SQUIRREL for simulated super-resolution images with no molecules missing with different SNR widefield images used as the reference. Error bars represent standard deviation of n=10 repeats. **i)** RSP values generated by SQUIRREL for super-resolution images with varying numbers of molecules missing when a noise-free widefield image is used as the reference. Error bars represent standard deviation of n=100 repeats. **j-m)** Mean RSP mapped for number of molecules removed against Δd for widefield reference images with **j)** no noise (n=100), **k)** SNR = 2 (n=10), **l)** SNR = 5 (n=10), **m)** SNR = 10 (n=10).

'Perfect' super-resolution images were simulated for different sized rings with all 8 molecules present, and artefactual super-resolution images were generated through random removal of various numbers of molecules from the ring (Fig. S7b-d). Widefield images with all 8 molecules present were also generated to serve as SQUIRREL reference images. These either feature no noise, or have one of three different signal-to-noise ratios (SNR) (Fig. S7e-g). When the super-resolution image contained no artefacts, the RSP values were dictated by the SNR of the reference image, with higher SNR yielding higher RSP values (Fig. S7h). The RSP does not significantly vary when changing the size of the ring structure for a constant SNR. Next, the sensitivity of SQUIRREL was assessed for artefactual super-resolution images with up to 5

molecules absent when compared with a noise-free reference image with all 8 molecules present (Fig. S7i). When there were no molecules removed from the super-resolution image, the RSP steadily increased with Δd; however, when molecules were removed from the super-resolution image the opposite relationship was observed, with the RSP decreasing at larger values of Δd. This relationship became more pronounced with greater numbers of removed molecules (i.e. more artefactual images). For Δd less than 100 nm, the RSP values were not significantly different to the perfect super-resolution images regardless of the number of molecules absent from the structure. This is due to the lack of resolution support in the widefield image. However, the RSP indicated the presence of artefacts at all larger Δd values. The larger error bars associated with the RSP values for increasingly artefactual super-resolution images are due to the random nature of multiple molecule removals. The relationship between the extent of image artefacts (i.e. number of missing molecules) and the size of the structure (i.e. Δd) is displayed in Fig. S7j. The combined effect of reference image SNR, extent of super-resolution image defects and structure size is plotted similarly in Fig. S7k-m. As in Fig. S7h RSP values are consistently lower for low SNR, and as in Fig. S7j there is higher variation in RSP values for more extreme defects and larger structures. Based on these results, we conclude that SQUIRREL is sufficiently sensitive to describe defects occurring on a scale down to ~150 nm, with even smaller scales possible for high SNR.

Supplementary Note 7: Super-resolution cross-validation

The resolution of the error maps produced by SQUIRREL is limited by the resolution of the reference image used. Therefore, in the case of a diffraction-limited reference, the resolution map will only highlight large scale artefacts (Sup. Note 6). It is possible, however, to cross-validate different super-resolution methods using a super-resolution (rather than diffraction-limited) reference. As a pilot sample we chose the prototypic poxvirus, vaccinia virus (VACV). The major infectious form of VACV, mature virions (MVs), are brick-shaped particles measuring 360x270x250 nm [15]. MVs are composed of three main viral substructures: a bi-concave dumbbell shaped core containing the viral genome, two proteinaceous structures termed lateral bodies sitting within the core concavities, and a single lipid bilayer membrane that encompasses these structures (Fig. S8a). We recently described these structures in detail using SIM and STED, mapping a subset of molecular constituents of the virus [36]. MVs provide an ideal test case for SQUIRREL as virion substructures cannot be discriminated by conventional fluorescence microscopy but are sufficiently large to be perceived as independent structures by most super-resolution methods.

To generate same field-of-view widefield, SIM, STED, maximum likelihood estimation (MLE) and SRRF images, recombinant viruses containing a GFP-tagged lateral body protein (and Alexa Fluor-647-tagged anti-GFP nanobodies for MLE and SRRF imaging) were bound to gridded coverslips and imaged using different optical devices. As various imaging modalities have different optical paths, the acquired images cannot be directly aligned due to optical aberrations. To correct this we have developed a non-rigid registration algorithm, provided in NanoJ-SQUIRREL, which captures the field distortion of each image against a reference (SIM image in this example, Fig. S8b). In multi-image elastic registration, the image is divided into a user-selected number of blocks (similarly to Fig. S9). For each block, an optimal $\Delta x,\Delta y$ translation is calculated such that local similarity between the block in the image currently being registered and the block in the reference image is maximised. This calculation is done by cross-correlation, in the same manner described in Sup. Note 3 (Stage A). If a block does not support sufficient correlation against its given reference block, $\Delta x,\Delta y$ will be predicted by interpolation based on the values of neighbouring blocks. An elastic translation matrix is then calculated by inverse distance weighting [45] and applied to the corresponding image by bi-cubic spline interpolation [38]. New images are thus generated where there is ideal uniform alignment between modalities. In Fig. S8c we show the evolution of error maps for a single virus when using widefield, SIM, STED or SRRF images as a reference. As lateral bodies are considerably smaller than the diffraction limit, when using a widefield reference image, defects could not be perceived with RSP values all approaching 1.0. Using a super-resolution reference however immediately highlights dissimilarities between the various super-resolution images. These errors reflect asymmetries and inconsistencies along and within lateral bodies; the RSP and RSE also suggest a non-linear intensity scaling across the super-resolution methods. Figure S8d-e shows the RSP and RSE value distributions of 90 viruses analysed from multiple fields-of-view. Interestingly, the range of values in these distributions demonstrates that there is a high degree of variability between super-resolution images generated by different methods. However, by applying SQUIRREL researchers have the potential to filter super-resolution datasets for structures with a high-degree of correlation across various methods prior to further analysis.

Ideally the user should have a high degree of confidence in the super-resolution method used to generate the reference image, else it becomes difficult to disentangle the contributions of the reference and super-resolution images to the error map. In the example shown here, the use of four different super-resolution strategies on the same sample can be examined to identify any conserved errors which appear endemic to one particular modality. If different labelling approaches are used for different super-resolution imaging methods, errors may be indicative of an inherent difference between the labels. Here we have used GFP to label the lateral bodies for SIM and STED imaging, and anti-GFP nanobodies tagged with Alexa Fluor 647 for SRRF and SMLM imaging; the error map thus may contain errors arising from e.g. GFP molecules that nanobodies have failed to bind to. However, in this case SQUIRREL could be used for further investigation and optimisation of the labelling. For example, in this case dual colour SIM imaging could be performed on the double-labelled lateral bodies with one channel used as the reference and another as the super-resolution image for samples prepared with various concentrations of anti-GFP nanobody.

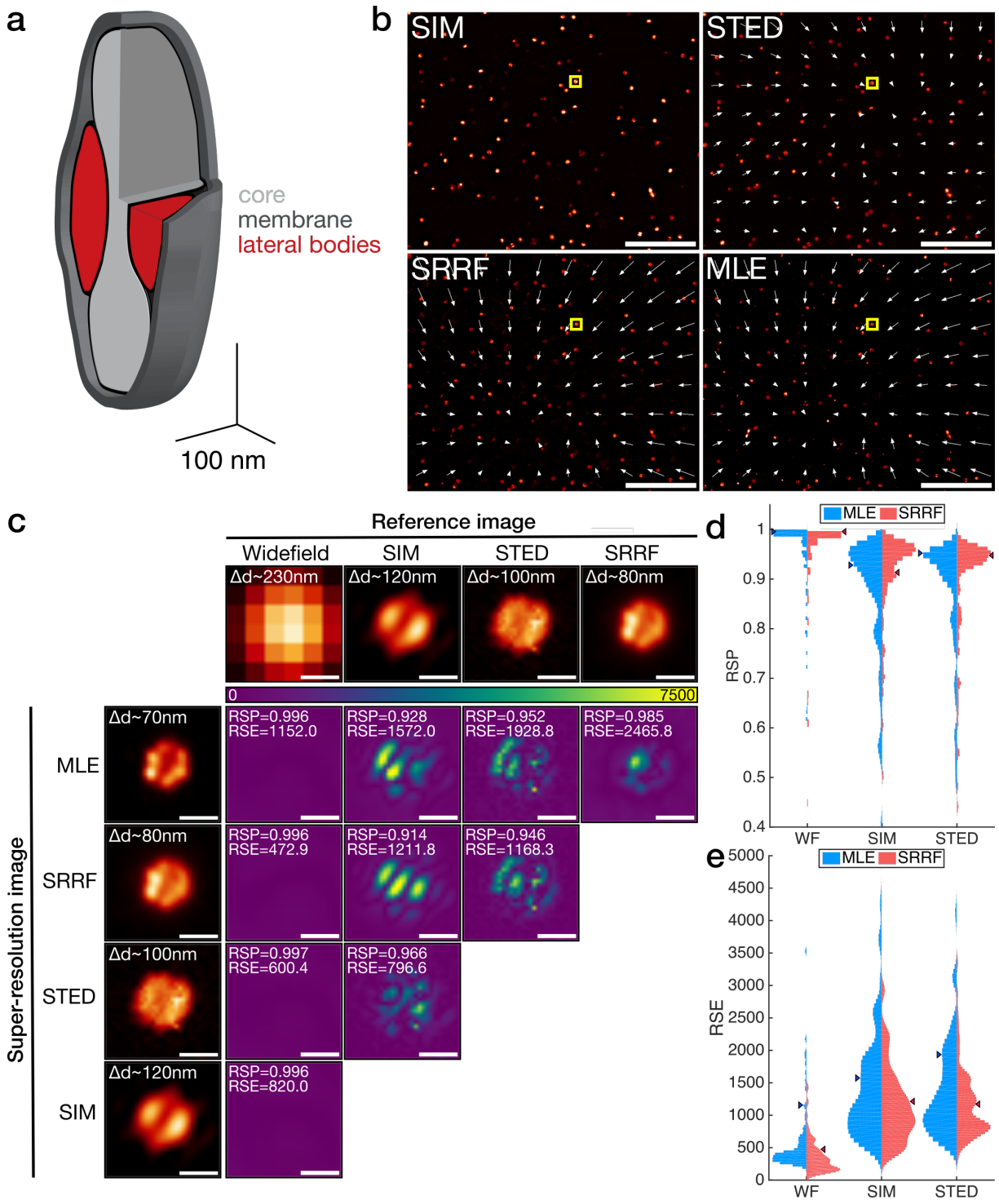

Fig. S8. Comparison of vaccinia virus lateral bodies imaged with different super-resolution modalities. a) Schematic of vaccinia structure, red highlights the lateral bodies with the remaining major structural components shown in grey. **b)** Field of vaccinia virus particles with GFP-labelled lateral bodies and Alexa Fluor-647 anti-GFP nanobodies imaged with SIM, STED and dSTORM for SRRF and MLE reconstructions. White arrows indicate the transformation used to align images from different modalities with the SIM image. Vector field magnitude was artificially increased 10-fold to aid visualisation. Scale bars = 5 μm. **c)** Cross-comparisons of the viral particle from the yellow box in **a**. Error maps are displayed for each of the super-resolution modalities when using the widefield images and any super-resolution images with lower resolution as the reference. Scale bars = 200 nm. **d)** Violin plots of RSP values when comparing MLE and SRRF reconstructions against widefield, SIM and STED reference images for n=90 individual viruses from the images in **b**. Arrowheads indicate values for the example virus in **c**. **e)** As in **d**, but RSE values. Figure represents data acquired from single experiment.

Supplementary Note 8: Image Fusion

Image fusion (provided within the NanoJ-SQUIRREL package) provides a super-resolution estimate merging the best traits of multiple super-resolution reconstructions through a weighted average. For this purpose, the fusion process weights the local information of each reconstruction according to its local error to achieve a final estimate of higher quality than any of its components. The process starts by the calculation of $R(n,x,y)$ as the root-mean-square-error (RMSE) of each reconstruction n for a small 3x3 window (Eq. S14). Here $M(n,x,y)$ corresponds to the error map matrix (Eq. S13) for the n-th super-resolution reconstruction provided. Next a matrix $R_{\max}(x,y)$ is also calculated, containing the maximum value of $R(n,x,y)$ for each pixel across N total reconstructions (Eq. S15). A weight matrix for each super-resolution reconstruction can then be calculated through Eq. S16 (note the truncation of the denominator to 1 in order to avoid a zero-division). For the $W(n,x,y)$ calculation we have chosen to use the RMSE over the 3x3 window as described in Eq. S14 instead of $M(n,x,y)$ directly to provide local error smoothing, minimising sharp pixel-wise changes between individual dominant pixels from each reconstruction. The final fusion image $I_{SF}(x,y)$ is generated through a weighted average (Eq. S17).

$$R(n,x,y) = \sqrt{\frac{1}{9}\sum_{i=-1}^{1}\sum_{j=-1}^{1} M(n,x+i,y+j)^2} \tag{S14}$$

$$R_{\max}(x,y) = \max(\{R(n,x,y): n = 1,\dots,N\}) \tag{S15}$$

$$W(n,x,y) = \frac{R_{\max}(x,y)}{\max(R(n,x,y),1)} \tag{S16}$$

$$I_{SF}(x,y) = \frac{\sum_{n=1}^{N} I_S(n,x,y)\times W(n,x,y)}{\sum_{n=1}^{N} W(n,x,y)} \tag{S17}$$

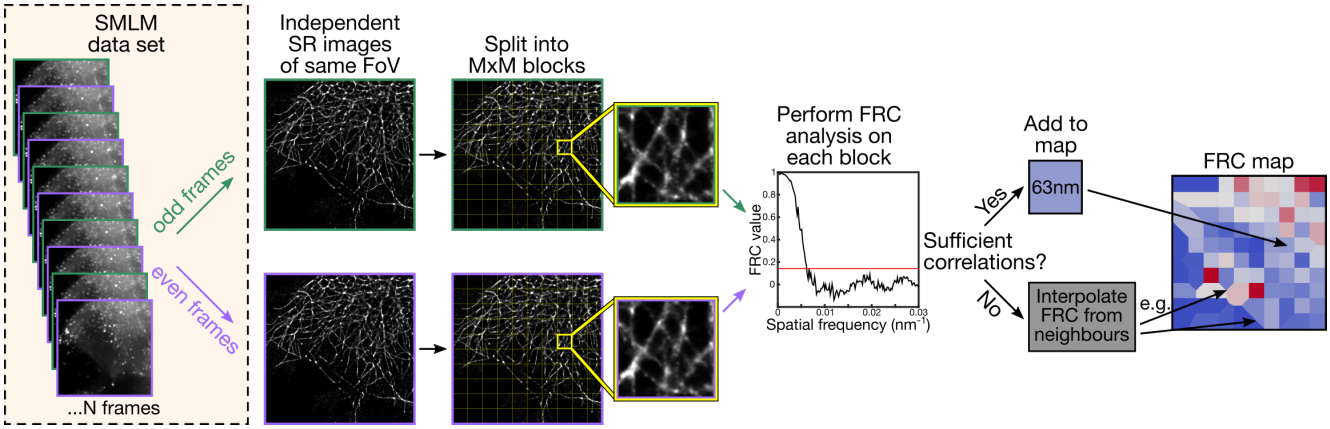

Fig. S9. FRC mapping. Resolution mapping by FRC is carried out by inputting two independent super-resolution images of the same field-of-view imaged under the same conditions. For the case of SMLM data, these two such images can be generated by splitting the data in half, for example by having odd and even frames producing two independent super-resolution reconstructions. Within the algorithm, the two data reconstructions are divided into blocks and for each block the FRC value is calculated as described in [16]. If sufficient correlations for FRC resolution estimation are found in a block, an equivalent region is colour coded to this value in an FRC resolution map. If not, the equivalent region is colour coded according to natural neighbour interpolation [46].

Supplementary Note 9: Optimising sample preparation for DNA-PAINT imaging of clathrin coated pits

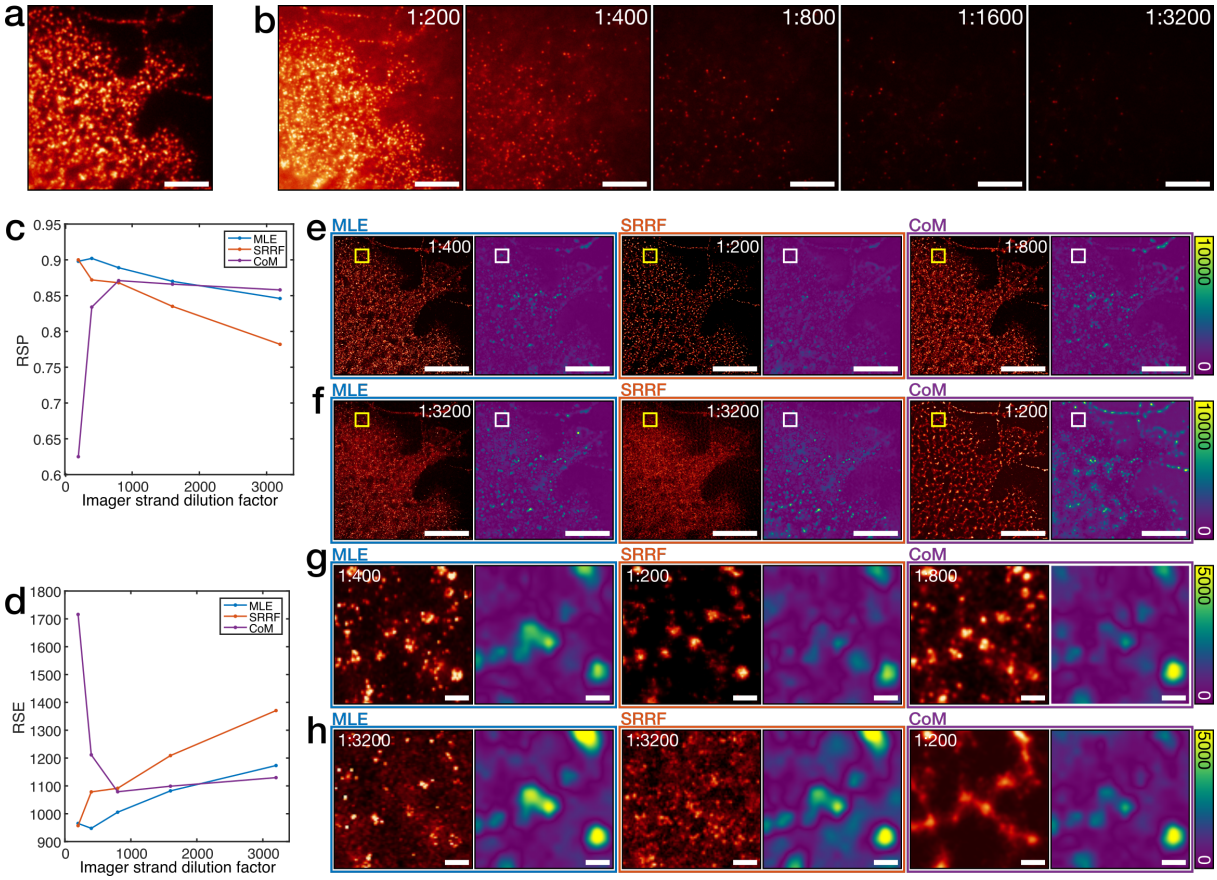

Fig. S10. Error analysis for optimisation of DNA PAINT labelling of clathrin-coated pits. a) Widefield image of clathrin-coated pits (CCPs). Scale bar = 5 µm. **b)** Example frames of the same region as imaged in a, but with dilutions of the imager strand at 1:200, 1:400, 1:800, 1:1600 and 1:3200. Scale bars = 5 µm. **c)** RSP values for MLE, SRRF and CoM reconstructions of the data sets with different imager strand dilutions. **d)** As in **c**, but RSE values. **e)** Super-resolution images and error maps from MLE, SRRF and CoM reconstructions at the best performing imager strand dilution as determined by the RSP values. Scale bars = 5 µm. **f)** As in **e**, but instead reconstructions are instead from the worst performing imager strand dilution. Scale bars = 5 µm. **g)** Insets from the boxed regions in **e**. Scale bars = 100 nm. **h)** Insets from the boxed regions in **f**. Scale bars = 100 nm. Figure represents data from 1 of 3 independent similar experiments.

Sample labelling is a major element influencing super-resolution imaging quality. SMLM methods in particular depend on labelling density and fluorophore photoswitching behaviour compatible with the analytical method chosen [5,14]. To ascertain if SQUIRREL image quality readouts can guide optimisation of sample labelling we applied SQUIRREL error analysis to DNA-PAINT based imaging. This method relies on the transient hybridization of complementary DNA templates; the 'docking' strand which is appended to the target protein and the fluorescently labelled 'imager' strand which is added to the sample media. When combined with SMLM reconstruction algorithms, it is possible to detect and localise these temporary immobilisation events as a fluorescent spot [47,48]. As bleached fluorophores are not permanently attached to the structure of interest, the on/off kinetics of DNA-PAINT are dictated by the concentration of imager strand utilized [23,49]. Thus we asked if SQUIRREL error analysis could be applied to determine the optimal imager strand concentration for super-resolution imaging of clathrin-coated pits (CCPs). CCPs appear as diffraction-limited spots in widefield microscopy images (Fig. S10a), and as 100-200 nm rounded pits by super-resolution microscopy [50]. Docking strand-labelled clathrin light chain was imaged for 20,000 frames using five different dilutions of imager strand (Fig. S10b). SQUIRREL was used to rank the quality of images produced using three different reconstruction algorithms; MLE, SRRF, and CoM. Interestingly, the quality of the reconstructed images depended on the combination of imager strand concentration and algorithm used, with the three algorithms showing optimal performance at different imager strand concentrations (Fig. S10c,d). Displayed in Figure S10e,f are the SQUIRREL-generated error maps for each algorithm at its most and least compatible imager strand concentrations, with magnified insets shown in Fig. S10g,h. These error maps illustrate the interdependence of sample preparation and algorithm choice as well as how sub-optimal sample preparation leads to increased errors and subsequent disappearance of structures (Fig. S10h, MLE), increased background signal (Fig. S10h, MLE, SRRF) and bridging between structures (Fig. S10, CoM). Collectively these results demonstrate the utility of

SQUIRREL to identify the optimal sample preparation and algorithm combination for a given SMLM experiment. It is important to note that for protein complexes or clusters of sizes similar to CCPs SQUIRREL will not be able to accurately defects on a sub-cluster scale (<150 nm, Sup. Note 6). For example, in the case of small protein clusters (<100 nm diameter) SQUIRREL will not be able to assess whether the size of these clusters is well-represented or if multiple small clusters are being anomalously fused together. However, this resolution limit of SQUIRREL can be bypassed if it is practical to use an alternative super-resolution method to generate a reference image (as in Fig. S8).

Supplementary Note 10: Improving image acquisition for dSTORM imaging of neuronal actin rings

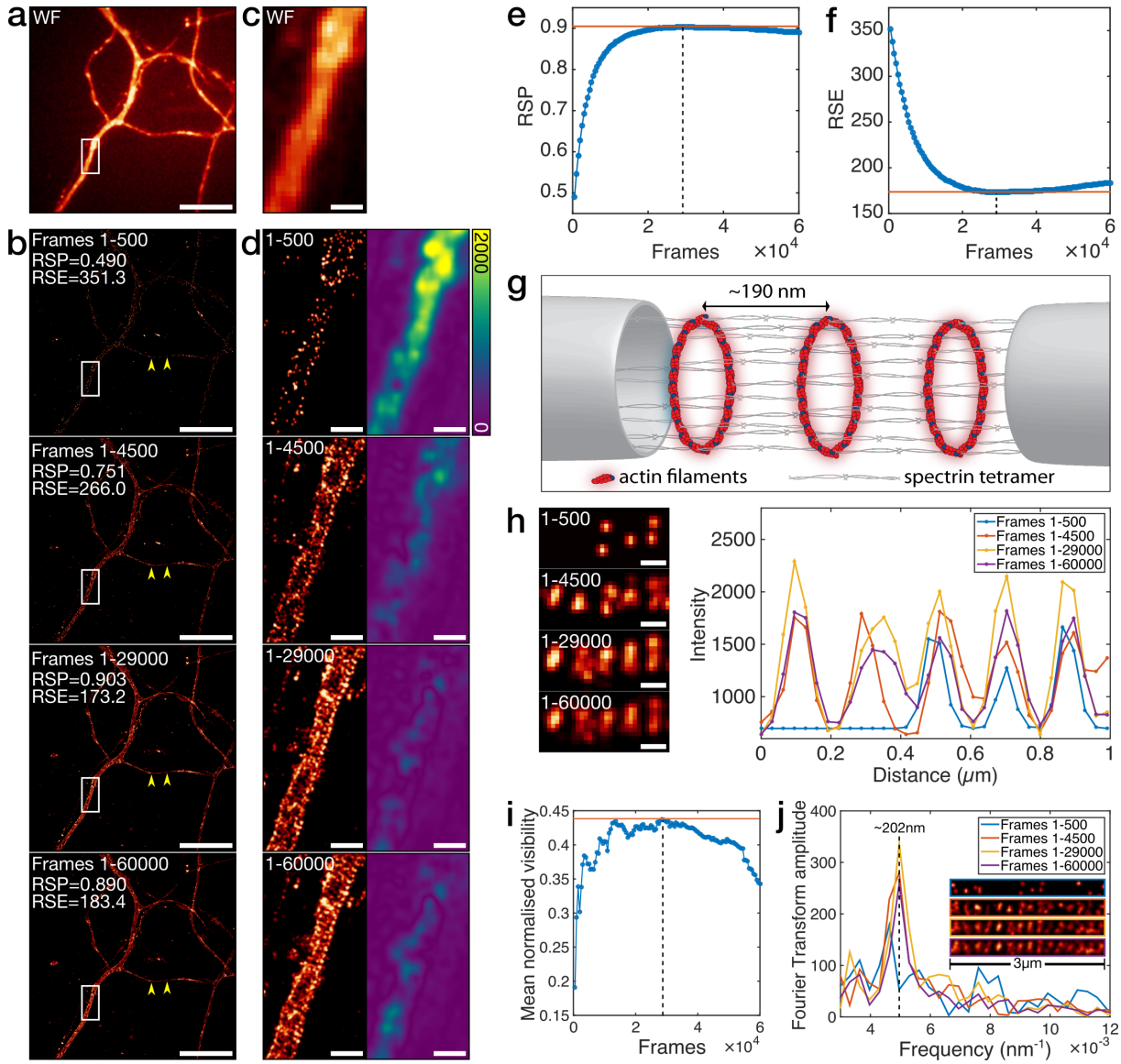

Fig. S11. Image quality assessment for informing number of frames for dSTORM imaging of neuronal actin rings. a) Widefield image of fixed neurons stained with phalloidin-Alexa Fluor 647. Scale bar = 10 μm. **b)** Super-resolution reconstructions of dSTORM data. The whole raw data set consisted of 60000 frames; four reconstructions are shown with localizations from the first 500 frames, first 4500 frames, first 29000 frames and all 60000 frames. RSP and RSE values were calculated with the widefield image in **a** acting as the reference. Scale bars = 10 μm. **c)** Enlarged view of the boxed region in **a**. Scale bar = 1 μm. **d)** Enlarged views of the boxed regions in **b** and corresponding error maps. Colour bar is consistent for each image. Scale bar = 1μm. **e)** RSP values for super-resolution images reconstructed from increasing numbers of frames. Dashed line indicates peak RSP value, obtained at 29000 frames. **f)** As in **e** but for RSE values. Dashed line indicates minimum RSE value, obtained at 29000 frames. **g)** Schematic showing the arrangement of actin rings and spectrin filaments within an axon. **h)** Left: 1 μm section of axon displaying periodic actin structures. Scale bars = 200 nm. Right: Line profiles of intensities (scaled to that of the widefield image) along this section of axon. **i)** Visibility analysis of the line profiles taken along the region in **h** with increasing numbers of frames. Dashed line indicates that the maximum visibility was obtained at 28500 frames. **j)** Fourier transforms of a 3 μm section of axon shown in the inset (from between the arrowheads in **b**). Figure represents single experiment.

Error mapping provides researchers with the means to quantitatively determine how different acquisition parameters may improve the quality of super-resolution images. To test this, a 60,000 frame dSTORM acquisition of sub-diffraction, periodically organized neuronal actin rings was acquired (Fig. S11) [24,51]. Particle localisation was performed, and the localisations used to generate 120 separate super-resolution reconstructions consisting of 500 to 60,000 frames (Fig. S11b). At low frame counts reconstructions showed no periodicity and the error maps exhibited large, widespread errors. As additional frames were included, reconstruction errors decreased and the expected repetitive pattern emerged (Fig. S11d).

Surprisingly, the RSP value peaked at 29,000 frames rather than converging at a maximum (Fig. S11e), while inclusion of more than 29,000 frames in the reconstruction led to a small decrease in the RSP value. The same trend was observed for the RSE value, which reached a minimum at 29,000 frames (Fig. S11f). To evaluate if the number of frames used for the super-resolution reconstruction had an impact on the visibility of structural details, we quantified the expected periodicity (200 nm) of the actin rings (Fig. S11g). Clearly defined periodicity emerged only when 29,000 or more frames were used for reconstruction (Fig. S11h). Consistent with this, the visibility index of actin rings (Fig. S11i, basis described in Online Methods and [14]) reached a maximum at 28,500 frames. Addition of more frames to the reconstructed super-resolution image resulted in deterioration of actin ring visibility. The RSP and RSE value peaks, validated by structural analysis, suggest that beyond this maximum quality peak point the unwanted contribution of free label and false detections is greater than the partially depleted correct structural labelling. Fourier analysis [51] of the 29,000 frame reconstruction was in agreement with previously reported values (Fig. S11j). These results indicate that a finite number of frames (29,000) as determined quantitatively by NanoJ-SQUIRREL were optimal for imaging neuronal actin rings, and that any frames acquired beyond this point did not improve image quality. Notably, this information has enormous potential for time-saving during both image acquisition and analysis for any repeatedly performed long acquisition. For the case demonstrated, the acquisition should be done in half the time achieving a higher quality than in a longer acquisition, with this estimation performed quantitatively instead of being based on a subjective human guess. We further performed a similar analysis calculating the evolution of resolution for the same dataset (through FRC calculation, Fig. S12). While FRC analysis indicates improved resolution as the number of frames is increased, the resolution stabilises if 29,000 or more frames are used without any deterioration in resolution beyond this point. Again, as in Fig. 2, this indicates that image resolution and image quality are weakly related, and that error mapping provides a more sensitive metric for data reliability.

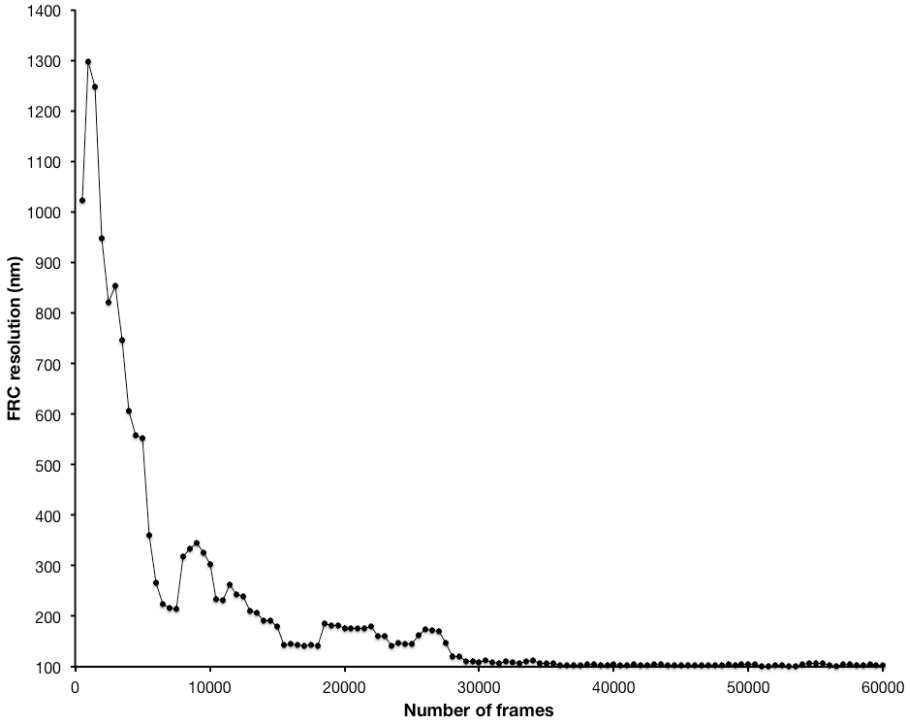

Fig. S12. Fourier Ring Correlation resolution for neuronal actin rings. Average FRC values for reconstructions obtained with an accumulating number of frames, in the same manner as Fig. S11e-f**.**

Supplementary References

[26] S. Deng, L. Liu, Y. Cheng, R. Li, Z. Xu, Effects of primary aberrations on the fluorescence depletion patterns of STED microscopy., Opt. Express. 18 (2010).

[27] L.H. Schaefer, D. Schuster, J. Schaffe, Structured illumination microscopy: artefact analysis and reduction utilizing a parameter optimization approach, J. Microsc. 216 (2004) 165–174. doi:10.1111/j.0022-2720.2004.01411.x.

[28] M. Erdélyi, J. Sinkó, R. Kákonyi, A. Kelemen, E. Rees, D. Varga, G. Szabó, Origin and compensation of imaging artefacts in localization-based super-resolution microscopy., Methods. 88 (2015) 122–32. doi:10.1016/j.ymeth.2015.05.025.

[29] T.J. Lambert, J.C. Waters, Navigating challenges in the application of superresolution microscopy., J. Cell Biol. 216 (2017) 53–63. doi:10.1083/jcb.201610011.

[30] D.R. Whelan, T.D.M. Bell, Image artifacts in Single Molecule Localization Microscopy: why optimization of sample preparation protocols matters, Sci. Rep. 5 (2015) 7924. doi:10.1038/srep07924.

[31] A. Burgert, S. Letschert, S. Doose, M. Sauer, Artifacts in single-molecule localization microscopy, Histochem. Cell Biol. 144 (2015) 123–131. doi:10.1007/s00418-015-1340-4.

[32] B. Zhang, J. Zerubia, J.-C. Olivo-Marin, Gaussian approximations of fluorescence microscope point-spread function models, Appl. Opt. 46 (2007) 1819. doi:10.1364/AO.46.001819.

[33] M.J. Rust, M. Bates, X.W. Zhuang, Sub-diffraction-limit imaging by stochastic optical reconstruction microscopy (STORM)., Nat. Methods. 3 (2006) 793–5. doi:10.1038/nmeth929.

[34] T.J. Gould, D. Burke, J. Bewersdorf, M.J. Booth, Adaptive optics enables 3D STED microscopy in aberrating specimens, Opt. Express. 20 (2012) 20998. doi:10.1364/OE.20.020998.

[35] D. Li, L. Shao, B.-C. Chen, X. Zhang, M. Zhang, B. Moses, D.E. Milkie, J.R. Beach, J.A. Hammer, M. Pasham, T. Kirchhausen, M.A. Baird, M.W. Davidson, P. Xu, E. Betzig, Extended-resolution structured illumination imaging of endocytic and cytoskeletal dynamics, Science (80-.). 349 (2015) aab3500-aab3500. doi:10.1126/science.aab3500.

[36] R.D.M. Gray, C. Beerli, P.M. Pereira, K.M. Scherer, J. Samolej, C.K.E. Bleck, J. Mercer, R. Henriques, VirusMapper: open-source nanoscale mapping of viral architecture through super-resolution microscopy., Sci. Rep. 6 (2016) 29132. doi:10.1038/srep29132.

[37] P. Wendykier, J.G. Nagy, Parallel Colt: A High-Performance Java Library for Scientific Computing and Image Processing., ACM Trans. Math. Softw. 37 (2011) 31–31:22. doi:10.1145/1824801.1824809.http.

[38] E. Catmull, R. Rom, A Class of Local Interpolating Splines, in: Comput. Aided Geom. Des., Elsevier, 1974: pp. 317–326. doi:10.1016/B978-0-12-079050-0.50020-5.

[39] M. Guizar-Sicairos, S.T. Thurman, J.R. Fienup, Efficient subpixel image registration algorithms., Opt. Lett. 33 (2008) 156–8. doi:10.1364/OL.33.000156.

[40] C.S. Smith, N. Joseph, B. Rieger, K.A. Lidke, Fast, single-molecule localization that achieves theoretically minimum uncertainty, Nat. Methods. 7 (2010) 373–375. doi:10.1038/nmeth.1449.

[41] J. Kennedy, R. Eberhart, Particle swarm optimization, in: Proc. ICNN'95 - Int. Conf. Neural Networks, IEEE, 1995: pp. 1942–1948. doi:10.1109/ICNN.1995.488968.

[42] Y. Shi, R. Eberhart, A modified particle swarm optimizer, in: 1998 IEEE Int. Conf. Evol. Comput. Proceedings. IEEE World Congr. Comput. Intell. (Cat. No.98TH8360), IEEE, 1998: pp. 69–73. doi:10.1109/ICEC.1998.699146.

[43] Z. Wang, A.C. Bovik, H.R. Sheikh, E.P. Simoncelli, Image quality assessment: From error visibility to structural similarity, IEEE Trans. Image Process. 13 (2004) 600–612. doi:10.1109/TIP.2003.819861.

[44] M. Palayret, H. Armes, S. Basu, A.T. Watson, A. Herbert, D. Lando, T.J. Etheridge, U. Endesfelder, M. Heilemann, E. Laue, A.M. Carr, D. Klenerman, S.F. Lee, Virtual-'Light-Sheet' Single-Molecule Localisation Microscopy Enables Quantitative Optical Sectioning for Super-Resolution Imaging, PLoS One. 10 (2015) e0125438. doi:10.1371/journal.pone.0125438.

[45] D. Shepard, A two-dimensional interpolation function for irregularly-spaced data, in: Proc. 1968 23rd ACM Natl. Conf. -, 1968: pp. 517–524. doi:10.1145/800186.810616.

[46] R. Sibson, A Brief Description of Natural Neighbour Interpolation, in: Interpret. Multivar. Data, 1981: p. 374.

[47] C. Flors, C.N.J. Ravarani, D.T.F. Dryden, Super-resolution imaging of DNA labelled with intercalating dyes, ChemPhysChem. 10 (2009) 2201–2204. doi:10.1002/cphc.200900384.

[48] I. Schoen, J. Ries, E. Klotzsch, H. Ewers, V. Vogel, Binding-activated localization microscopy of DNA structures., Nano Lett. 11 (2011) 4008–11. doi:10.1021/nl2025954.

[49] J. Schnitzbauer, M.T. Strauss, T. Schlichthaerle, F. Schueder, R. Jungmann, Super-resolution microscopy with DNA-PAINT, Nat. Protoc. 12 (2017) 1198–1228. doi:10.1038/nprot.2017.024.

[50] S.A. Jones, S.-H. Shim, J. He, X. Zhuang, Fast, three-dimensional super-resolution imaging of live cells., Nat. Methods. 8 (2011) 499–508. doi:10.1038/nmeth.1605.

[51] K. Xu, G. Zhong, X. Zhuang, Actin, Spectrin, and Associated Proteins Form a Periodic Cytoskeletal Structure in Axons, Science (80-.). 339 (2013) 452–456. doi:10.1126/science.1232251.